Ann. Geophys., 28, 2059–2069, 2010
www.ann-geophys.net/28/2059/2010/
doi:10.5194/angeo-28-2059-2010

Annales Geophysicae

Equatorial spread F fossil plumes

J. Krall[1], **J. D. Huba**[1], **S. L. Ossakow**[2], **and G. Joyce**[3]

[1]Plasma Physics Division, Naval Research Laboratory, Code 6790, 4555 Overlook Ave., SW, Washington, D.C., 20375-5000, USA
[2]Berkeley Research Associates, Beltsville, MD 20705-1434, USA
[3]Icarus Research, Inc., P.O. Box 30780, Bethesda, MD 20824-0780, USA

Received: 19 March 2010 – Revised: 15 October 2010 – Accepted: 31 October 2010 – Published: 9 November 2010

Abstract. Behaviour of equatorial spread F (ESF) fossil plumes, i.e., ESF plumes that have stopped rising, is examined using the NRL SAMI3/ESF three-dimensional simulation code. We find that fossil bubbles, plasma density depletions associated with fossil plumes, can persist as high-altitude equatorial depletions even while being "blown" by zonal winds. Corresponding airglow-proxy images of fossil plumes, plots of electron density versus longitude and latitude at a constant altitude of 288 km, are shown to partially "fill in" in most cases, beginning with the highest altitude field lines within the plume. Specifically, field lines upon which the $\boldsymbol{E}$ field has fallen entirely to zero are affected and only the low altitude ($\leq$600 km) portion if each field line fills in. This suggests that it should be possible to observe a bubble at high altitude on a field line for which the corresponding airglow image no longer shows a depletion. In all cases ESF plumes stop rising when the flux-tube-integrated ion mass density inside the upper edge of the bubble is equal to that of the nearby background, further supporting the result of Krall et al. (2010b).

Keywords. Ionosphere (Equatorial ionosphere; Ionosphere-atmosphere interactions; Ionospheric irregularities)

1 Introduction

Equatorial spread F (ESF), the result of a Rayleigh-Taylor-like instability in the night time ionospheric F-layer (Haerendel, 1974; Ossakow, 1981; Kelley, 1989; Hysell, 2000), has deleterious affects on electromagnetic signals. For example, ESF was discovered because it causes "diffuse echoes from the F-region of the ionosphere received continuously at night in equatorial regions over a wide range of wave-frequency" (Booker and Wells, 1938). At times, the strong electron density gradients associated with ESF degrade global communication and navigation systems (de La Beaujardiere et al., 2004; Steenburgh et al., 2008). Recently, the use of sophisticated three-dimensional computer simulation models (Huba et al., 2008; Retterer, 2010) has increased our basic understanding of ESF. Computer simulations have provided newly detailed explanations of numerous ESF-related phenomena including compositional (Huba et al., 2009b) and temperature signatures (Huba et al., 2009a) of ESF, ESF stabilization by meridional winds (Krall et al., 2009a; Maruyama et al., 2009; Abdu et al., 2006), the effect of zonal winds on ESF plume morphology (Huba et al., 2009c), ESF airglow (Krall et al., 2009b), and ESF-related "plasma blobs" (Krall et al., 2010a).

Radar backscatter observations show that an ESF plume can persist for hours after it has halted its upward motion with correspondingly persistent effects on co-located electromagnetic signals (Yokoyama et al., 2007). Plumes that have halted their upward motion are called "fossils" (Argo and Kelley, 1986; Mendillo et al., 1992; Schunk and Sojka, 1996; Makela, 2006; Sekar et al., 2007).

In this paper, we use the SAMI3/ESF three-dimensional simulation model (Huba et al., 2008) to study the properties and signatures of fossil ESF plumes and the effect of winds that transport these phenomena across the geomagnetic field in the zonal direction. We also consider the case in which a converging zonal wind acts to halt the upward rise of an ESF bubble, leading to a fossil.

This study is a follow-on to two previous studies. In one we showed that, in the case of zero neutral winds, an ESF bubble stops rising and becomes a fossil when the flux-tube-averaged ion mass density at the upper edge of the bubble rises to the point that it is equal to the corresponding ambient value (Krall et al., 2010b). We further showed that a fossil bubble continues to persist and evolve for hours after it has stopped rising. In another (Krall et al., 2009b), we found

Correspondence to: J. Krall
(jonathan.krall@nrl.navy.mil)

that a converging zonal wind can lead to the occurrence of a fossil bubble at lower heights and earlier simulation times than would otherwise occur. We found that such bubbles are accompanied by a unique airglow signature, but did not relate this finding to other modelling or observations of fossil plumes or bubbles. The aim of the present study is to describe simulations of various cases in which fossil plumes are expected to occur and to do so in enough detail that these findings can be verified through simultaneous in situ, radar, and/or airglow observations. Here we are particularly interested in the effects of winds.

We find that ESF plumes that have stopped rising often contain regions with persistent, but relatively weak, electric fields and that these regions show a distinct airglow signature. In particular, field lines that support these persistent $\boldsymbol{E}$ fields continue to show airglow depletions even while other parts of the same ESF airglow depletion are "filling in." We find that fossil plumes and corresponding plasma density depletions are transported by zonal winds, as observed, and that the density, electric field and airglow signatures found in the zero-wind simulation also occur for wind-transported ESF plumes. We show that a plume that is interrupted by converging zonal winds, resulting in a fossil, has an electric field that falls everywhere to zero, so that the entirety of the associated airglow depletion slowly fills in. In this case the airglow depletion might appear to fade out entirely while a plasma density depletion on the same field line persists at higher altitudes. Finally, we show that a weakly growing plume can attain a fossilized state where the $\boldsymbol{E}$ field is everywhere weak but persistent, resulting in a weak but persistent depletion at the airglow layer.

2 SAMI3 simulations

The NRL 3-D ionosphere code SAMI3/ESF (Huba et al., 2008) is used in this analysis. SAMI3/ESF is a version of the SAMI3 global ionosphere code (Huba et al., 2000, 2005) that has been modified for the study of ESF. SAMI3 models the plasma and chemical evolution of seven ion species (H^+, He^+, N^+, O^+, N_2^+, NO^+ and O_2^+). The complete ion temperature equation is solved for three ion species (H^+, He^+ and O^+) as is the electron temperature equation. Ion inertia is included in the ion momentum equation for motion along the geomagnetic field and $\boldsymbol{E}\times\boldsymbol{B}$ drifts are computed to obtain motion transverse to the field. Neutral composition and temperature are specified using the empirical NRLMSISE00 model (Picone et al., 2002). The version of SAMI3 used here and in our other recent ESF studies (Huba et al., 2008, 2009a,b,c; Krall et al., 2009a,b, 2010a,b) includes a perpendicular electric field $\boldsymbol{E}_\perp = -\nabla\Phi$ that is computed self-consistently to determine the $\boldsymbol{E}\times\boldsymbol{B}$ drifts.

The SAMI3/ESF potential equation is derived from current conservation ($\nabla\cdot\boldsymbol{J}=0$) in dipole coordinates (s,p,ϕ) and is similar to that derived in Haerendel et al. (1992):

$$\frac{\partial}{\partial p}\Sigma_{pp}\frac{\partial\Phi}{\partial p}+\frac{\partial}{\partial\phi}\Sigma_{p\phi}\frac{\partial\Phi}{\partial\phi}=\frac{\partial F_{\phi g}}{\partial\phi}+\frac{\partial F_{pV}}{\partial p} \quad (1)$$

where $F_{\phi g}=\int(r_{\rm E}\sin^3\theta/\Delta)(B_0/c)\sigma_{Hc}g_p\,ds$, and $F_{pV}=\int r_{\rm E}\sin\theta(B_0/c)\sigma_P V_{n\phi}\,ds$. Here, Φ is the electrostatic potential, g_p is the component of gravity perpendicular to $\mathbf{B}$, σ_P is the Pedersen conductivity,

$$\sigma_{Hc}=\sum_i\frac{n_i ec}{B\Omega_i}\frac{1}{1+\nu_{\rm in}^2/\Omega_i^2} \quad (2)$$

is the ion component of the Hall conductivity divided by the ion cyclotron frequency, $\Sigma_{pp}=\int(p\Delta/b_s)\sigma_P\,ds$, $\Sigma_{p\phi}=\int(1/pb_s\Delta)\sigma_P\,ds$, $\Delta=(1+3\cos^2\theta)^{1/2}$, $\Omega_i=eB/m_ic$, $\nu_{\rm in}$ is the ion-neutral collision frequency, B is the local geomagnetic field, B_0 is the geomagnetic field at the equator, θ is the magnetic colatitude, $b_s=(r_{\rm E}^3/r^3)\Delta$, $r_{\rm E}$ is the radius of the earth, and field-line integrations with respect to coordinate s are along the entire field line, with the base of the field lines being at 85 km. Equation (1) has been simplified by neglecting Hall-conductance terms relative to Pedersen-conductance terms on the LHS (e.g., $\Sigma_H=\sigma_H=0$), neglecting the $\partial F_{pg}/\partial p$ term relative to the $\partial F_{\phi g}/\partial\phi$ term on the RHS, and by setting the meridional wind to zero. Examples of the potential equation without these simplifications appear in Krall et al. (2009b) and, in the context of the SAMI3 code, Huba et al. (2010).

The 3-D simulation model is initialized using results from the two-dimensional SAMI2 code. SAMI2 is run for 48 h using the following geophysical conditions: F10.7 = 75, F10.7A = 75, Ap = 4, and day-of-year 80 (e.g., 21 March 2002). The simulation is centered at geographic longitude 0° so universal time and local time are the same. The $\boldsymbol{E}\times\boldsymbol{B}$ drift in SAMI2 is prescribed by the Fejer/Scherliess model (Scherliess and Fejer, 1999). The plasma parameters (density, temperature, and velocity) at time 19:20 UT (of the second day) are used to initialize the 3-D model at each magnetic longitudinal plane.

The 3-D model uses a non-uniform, non-orthogonal numerical grid that follows the geomagnetic field. The simulation region includes field lines with magnetic apex heights from 90 km to 2400 km, and longitudes from −2° to 2° (longitudinal width of 4° or ≃ 460 km). The plasma is modelled from hemisphere to hemisphere up to ±31° magnetic latitude. Except where noted, the grid is $(n_{\rm z},n_{\rm f},n_{\rm l})$ = (101, 202, 96), where $n_{\rm z}$ is the number of grid points along the magnetic field, $n_{\rm f}$ is the number of "field lines," and $n_{\rm l}$ is the number of longitudes. This grid has a resolution of ∼6 km × 5 km in altitude and longitude in the magnetic equatorial plane. The numerical grid is periodic in longitude. In essence we are simulating a narrow "wedge" of the ionosphere in the post-sunset period. Unless noted, the ESF instability in each simulation was initiated by imposing a Gaussian-like perturbation in the plasma density at the initial time (19:20 UT): a peak density perturbation of 15% centered at 0° longitude with a half-width of 0.25°, and at an altitude $z=300$ km with a half-width of 50 km. This seed perturbation extends along the

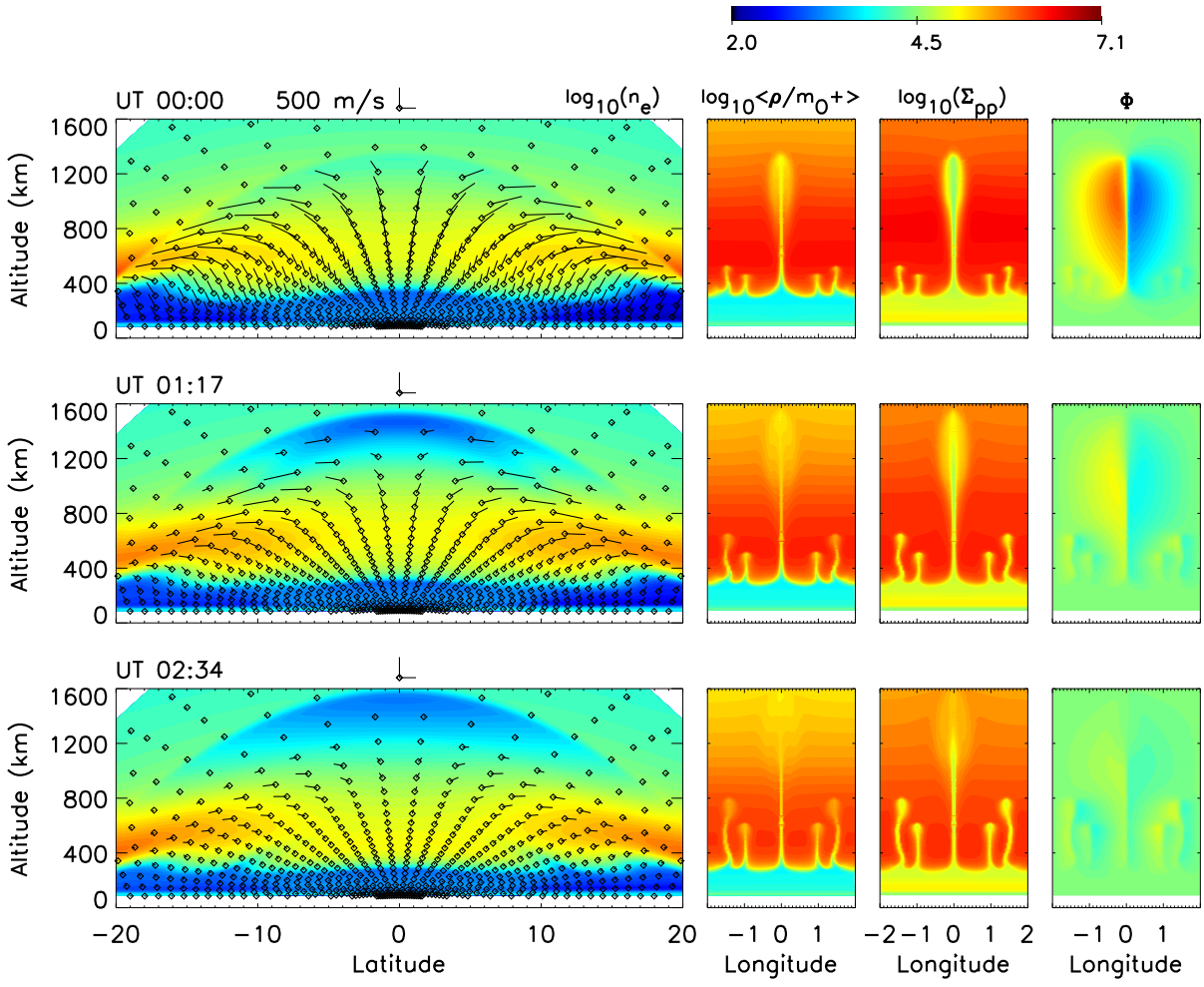

Fig. 1. Left: Contours of $\log_{10} n_e$ versus height and latitude at longitude 0 at various times. Right three columns: Contours of the log of the flux-tube averaged ion mass density ($\log_{10}\langle\rho/m_{O^+}\rangle$), the log of the Pedersen conductance ($\log_{10}(\Sigma_{pp})$) and the electrostatic potential, plotted in the equatorial plane. Number densities for n_e, and $\langle\rho/m_{O^+}\rangle$, are in units of cm^{-3} and correspond to the color-bar scale. In the left hand panels, O^+ ion velocity vectors indicate the direction of flow *away* from the dot. Here there are no winds.

entire flux tube. For this study, the vertical and meridional neutral winds are set to zero and the zonal neutral wind is set either to zero, to a constant 100 m s^{-1} or to a time-dependent converging wind pattern with peak velocities $\pm$10 m s^{-1}.

3 The development of a fossil bubble

Figure 1 shows an example of a simple ESF bubble viewed in a constant longitude plane (left panels). Here the zonal wind is set to zero. The smaller right-hand panels in this figure show contours of the log of the flux-tube averaged mass density normalized to the O^+ mass $\log_{10}\langle\rho/m_{O^+}\rangle$, the log of the Pedersen conductance $\log(\Sigma_{pp})$, and the electrostatic potential Φ plotted in the equatorial plane. The average mass density, which is reduced within an active, upwardly drifting bubble, indicates the shape and extent of the bubble that is shown as contours of $\log_{10}(n_e)$ in the left hand panels. The left-hand panel shows the motion of O^+ ions (both $\boldsymbol{E}\times\boldsymbol{B}$ drifts and field-aligned flows), where velocity vectors indicate the direction of flow *away* from the dot in each case. In this simulation there are no winds ($V_{n\phi}=0$).

This simulation was described in Krall et al. (2010a), where it was shown that the upward motion of the bubble stops when $\langle\rho\rangle$ at the upward edge of the bubble is the same as that of the nearby background ionosphere at the same height. Here we describe this result in further detail. We first note the sequence of events shown in Fig. 1. In the upper row of contour plots (00:00 UT), the bubble is active. This is indicated by ion flow vectors that extend outward across field lines (the dots in each left-hand panel are arrayed along geomagnetic field lines), by $\langle\rho\rangle$ values within the bubble that are lower than background values, and by a strong zonal gradient in the electrostatic potential. As noted in Huba et al. (2009b)

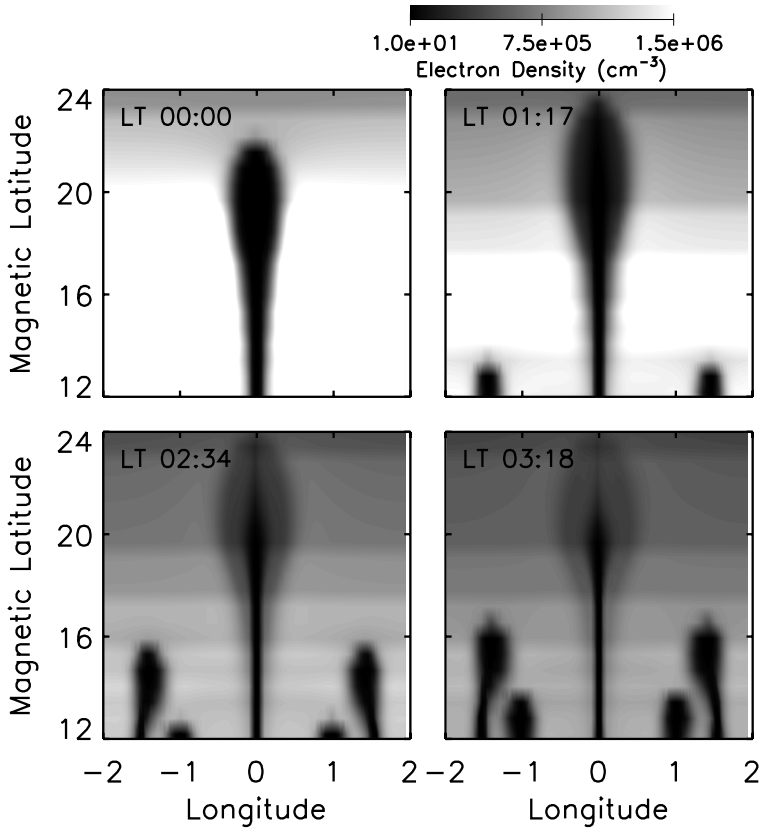

Fig. 2. Electron density versus longitude and latitude at a constant altitude of 288 km at various times. The first three time values correspond to those shown in Fig. 1. The latitude range lies in northern half of the simulation.

and Krall et al. (2010a), a "super fountain effect" acts within an ESF bubble, producing density crests at altitude 600 km and latitude $\pm 16^\circ$ that are analogous to the background "Appleton anomaly" ionization crests. In the middle row of contour plots (01:17 UT), the bubble has nearly halted its upward motion. This is indicated by ion flow vectors near the top of the bubble that are almost entirely parallel to the geomagnetic field (on lower altitude field lines, upward $\boldsymbol{E} \times \boldsymbol{B}$ drifts are more prevalent), by $\langle \rho \rangle$ at the top of the bubble that is close to background values, and by a nearly-zero zonal gradient in the electrostatic potential at the height of the bubble apex. Here the density crests within the bubble (altitude 500 km, latitude $\pm 18^\circ$) have fallen to lower altitude and have grown stronger as plasma drains from the bubble apex.

In the lower row of Fig. 1 (02:34 UT), the bubble has reached a largely-quiescent fossil state, with minimal plasma motion in the upper part of the bubble, where a density depletion persists. On these outer field lines, which we refer to as the "head" of the bubble, the plasma density at altitudes of 300–700 km is now similar to that of the background ionosphere. As a result, the Pedersen conductance Σ_{pp} is also nearly equal to that of the background ionosphere. On lower altitude field lines within the bubble, the "stalk" of the bubble, we find that a weak electric field persists along with low values of $\langle \rho \rangle$ and Σ_{pp}, relative to the background. We note that the 7 h of simulation time that have passed in order for the bubble to obtain a fossil state is probably an overestimate. Simulations of bubbles in a global context by Huba and Joyce (2010) show that perturbations that are imposed as early as 17:00 local time can lead to growing ESF bubbles.

Further results from this same simulation are shown in Fig. 2. As a proxy for the airglow images that have been used in the past to study ESF depletions (see, e.g., Makela, 2006), we show contours of electron density versus longitude and latitude at a constant altitude of 288 km at various times, the first three of which correspond to those of Fig. 1. The altitude 288 km is used because it lies in the altitude range, 250–300 km, that is typically the source of 630.0 nm airglow. The latitude range of Fig. 2 is in the northern half of the simulation. As the simulated ESF depletion increases in height, it extends northward (and southward) in latitude, moving further into the field of view of Fig. 2. As the bubble obtains a fossil state it first stops moving outward in latitude (01:17 UT). The highest latitude areas of depletion then begin to fill in (02:34 UT) as the plasma density within the bubble falls further downward (see Fig. 1, lower left panel). At the end of the simulation (03:18 UT) the upper part (head) of the airglow depletion has filled in while the airglow signature of the stalk remains dark.

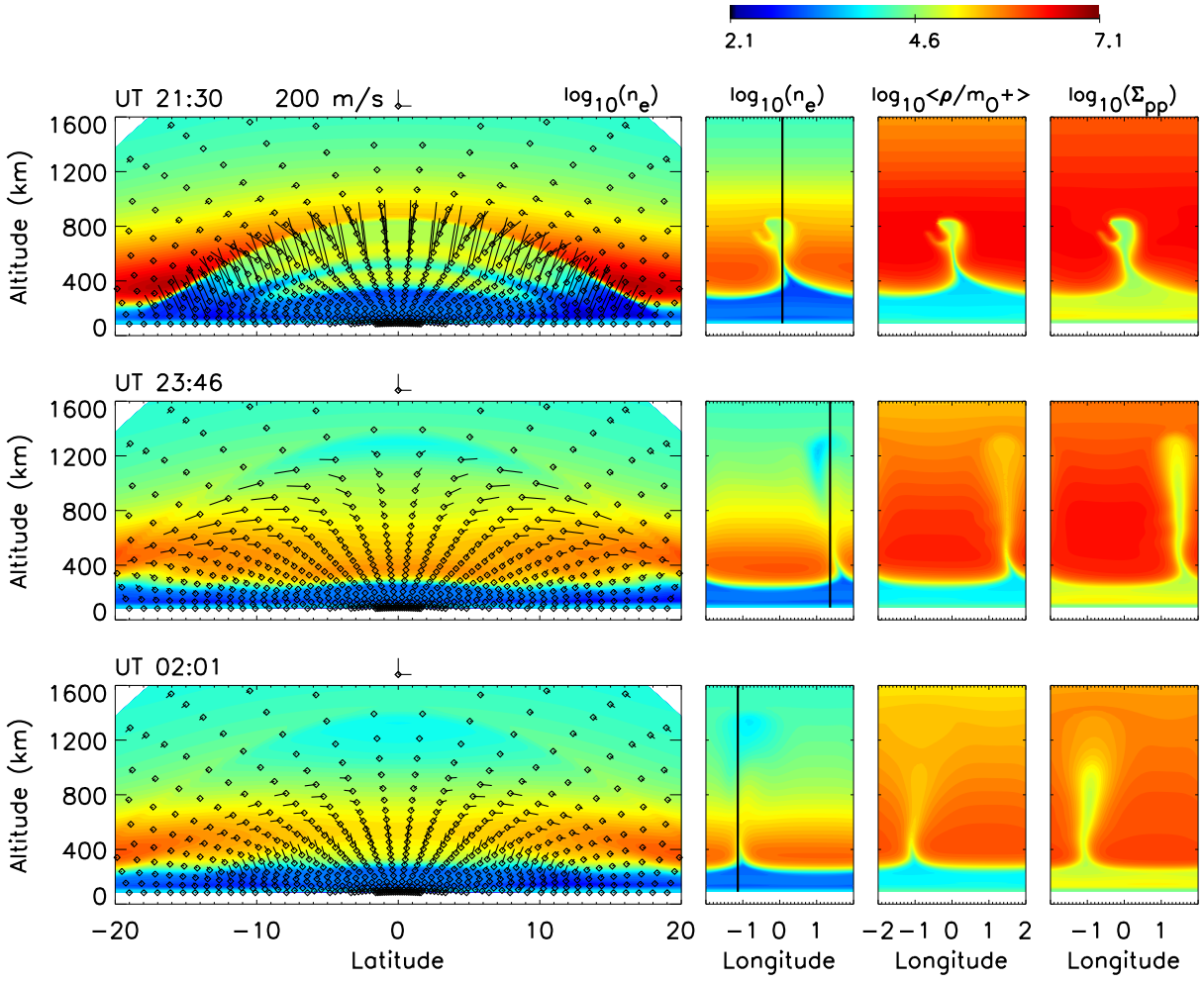

Fig. 3. Left: Contours of $\log_{10} n_e$ versus height and latitude at various times. Right three columns: Contours of $\log_{10} n_e$, the log of the flux-tube averaged ion mass density ($\log_{10}\langle\rho/m_{O^+}\rangle$) and the log of the Pedersen conductance ($\log_{10}(\Sigma_{pp})$), plotted in the equatorial plane. Number densities for n_e, and $\langle\rho/m_{O^+}\rangle$, are in units of cm^{-3} and correspond to the colour-bar scale. In the left hand panels, O^+ ion velocity vectors indicate the direction of flow *away* from the dot. This case includes a constant, eastward zonal wind of 100 m s^{-1}.

Our basic findings are that the airglow signature can decay even while the bubble persists and that a persistent airglow signature is associated with persistent, if weak, $\boldsymbol{E}$ fields. The collapse of the electric field in the head of the bubble at late times is associated with a "filling in" of both the Pedersen conductance and the simulated airglow depletion.

4 The effect of a zonal wind on a fossil bubble

Figures 3 and 4 show a repeat of the simulation of Figs. 1 and 2 but with a constant eastward 100 m s^{-1} zonal neutral wind imposed. As described by Zalesak et al. (1982), zonal winds act on the density gradients of an ESF bubble so as to transport the bubble in the direction of the wind, albeit with a velocity below that of the wind velocity. In order to accurately capture this transport, the number of zonal grid points was increased from 96 to 192 for this simulation.

Shown in Fig. 3 is the bubble viewed in a constant longitude plane (left panels) as contours of $\log_{10}(n_e)$ at various times. As in Fig. 1, O^+ motion is shown by velocity vectors that indicate the direction of flow *away* from the dot in each case. The smaller right-hand panels in this figure show contours of the log of the electron density in the equatorial plane $\log_{10} n_e$, the flux-tube averaged mass density normalized to the O^+ mass $\log_{10}\langle\rho/m_{O^+}\rangle$, and the log of the Pedersen conductance $\log(\Sigma_{pp})$. The location in longitude for each left-hand panel is indicated by a vertical line in the corresponding plot of $\log_{10} n_e$ versus longitude and altitude. Figure 3 shows bubbles that are tilted towards the western direction in comparison to the zero-wind result of Fig. 1, which shows no tilt. Without a realistic wind pattern, as was used in Huba et al. (2009c), commonly-observed "C" shaped plumes are not obtained.

Further results from this same simulation are shown in Fig. 4, where contours of electron density versus longitude

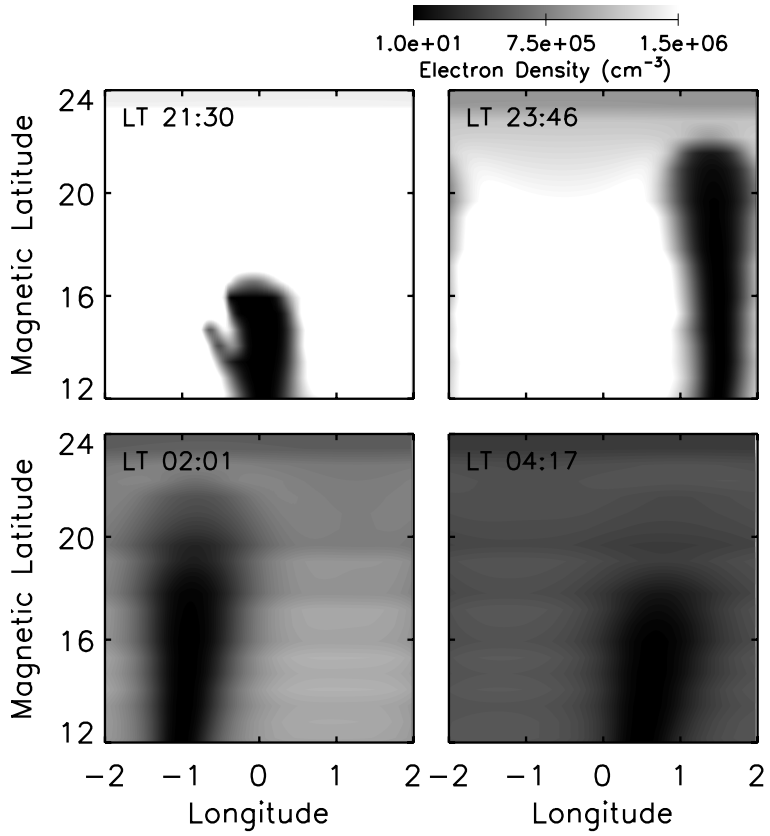

Fig. 4. Electron density versus longitude and latitude at a constant altitude of 288 km at various times. The first three time values correspond to those shown in Fig. 3.

and latitude are plotted at a constant altitude of 288 km at various times, the first three of which correspond to those of Fig. 3. Time values for the three rows of Fig. 3 and the first three panels of Fig. 4 were chosen to show configurations similar to those of Fig. 1: an active bubble, a bubble that has nearly halted, and a fossil bubble that has evolved for some time.

The key result of this simulation is that the findings in the simple zero-wind simulation also hold for the more realistic case where a zonal wind transports the fossil bubble even as vertical and field-aligned ion motion within the bubble are decaying, first in the head of the plume and then in the stalk. As expected, the presence of the zonal wind results in a bubble that does not rise as quickly as in the zero-wind case (Zalesak et al., 1982). As in the zero-wind simulation, the airglow signature of the head fades as, simultaneously, the Pedersen conductance increases and the plasma drifts fall virtually to zero.

As is seen in radar observations, the fossil density depletion above the F-layer persists even as it is distorted by its interaction with the zonal wind. Because the simulation does not use a high-order, non-diffusive transport scheme, neither the active (e.g., 21:30 UT) nor the fossil depletion show the bifurcations that are evident in such simulations (see, e.g., Huba and Joyce, 2007).

5 The effect of a converging zonal wind

As shown in Figs. 5 and 6, we repeat once again the simulation of Figs. 1 and 2 but with a very mild (10 m s^{-1}) converging zonal wind imposed, beginning at 22:00 UT and reaching full force at 23:00 UT. The wind is zero at the edges of the simulation ($\pm 2^\circ$ longitude) and ramps up to full speed (± 10 m s^{-1}) at the center of the simulation. In other words, the wind is eastward for longitudes < 0 and westward for longitudes > 0 (the wind pattern does not vary with height and corresponding meridional winds are neglected). This wind pattern is simular to that used in Krall et al. (2009b) and, as in that study, the wind has the effect of halting the upward motion of the ESF bubble at an earlier time and a lower altitude than in an otherwise-identical simulation with no winds.

Shown in Fig. 5 is the bubble viewed in a constant longitude plane (left panels) as contours of $\log_{10}(n_e)$. The smaller right-hand panels show contours of the flux-tube averaged mass density normalized to the O^+ mass $\log_{10}\langle\rho/m_{O^+}\rangle$, the log of the Pedersen conductance $\log(\Sigma_{pp})$, and the

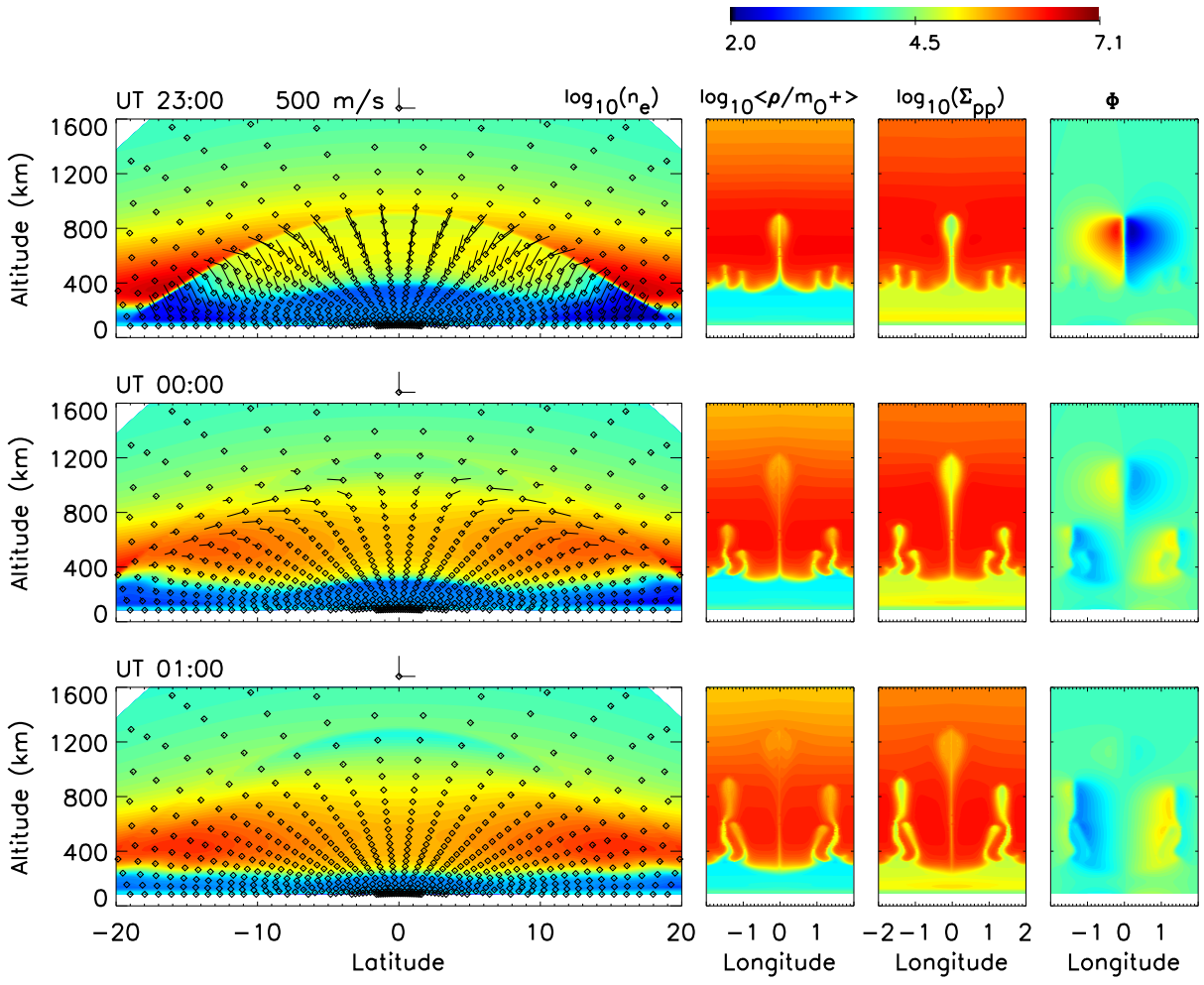

Fig. 5. Left: Contours of $\log_{10} n_e$ versus height and latitude at longitude 0 at various times. Right three columns: Contours of the log of the flux-tube averaged ion mass density ($\log_{10}\langle\rho/m_{O^+}\rangle$), the log of the Pedersen conductance ($\log_{10}(\Sigma_{pp})$) and the electrostatic potential, plotted in the equatorial plane. Number densities for n_e, and $\langle\rho/m_{O^+}\rangle$, are in units of cm^{-3} and correspond to the colour-bar scale. In the left hand panels, O^+ ion velocity vectors indicate the direction of flow *away* from the dot. This case includes a converging zonal wind of $\pm 10\,m\,s^{-1}$.

electrostatic potential Φ plotted in the equatorial plane. As in Figs. 1 and 3, O^+ motion is plotted via velocity vectors that indicate the direction of flow *away* from the dot in each case.

Airglow-proxy results from this simulation are shown in Fig. 6, where contours of electron density versus longitude and latitude are plotted at a constant altitude of 288 km at various times, the first three of which correspond to those of Fig. 5. Once again, time values for the three rows of Fig. 5 and the first three panels of Fig. 6 were chosen to show specific states of the evolving bubble: an active bubble, a bubble that has nearly halted, and a fossil bubble that has evolved for some time.

The key difference between these results and those of Figs. 1 and 2 is that the converging wind has had the effect of reducing and then stopping upward $\boldsymbol{E} \times \boldsymbol{B}$ drifts throughout the bubble; in the other cases, this effect is limited to the head of the bubble. Figure 6 notably differs from Figs. 2 and 4 in that the airglow signature of the entire depletion fades instead of only the upper part. As in the other cases above, the plasma density depletion at high altitudes persists as the bubble becomes a fossil.

6 Fossils resulting from weakly-growing bubbles

Finally, we repeat the simulation of Figs. 1 and 2 but with the instability seeded via random fluctuations in the O^+ density, temperature, and velocity. As in Krall et al. (2010a) these initial fluctuations are based on the observed amplitudes of traveling ionospheric disturbances as reported in Hocke and Schlegel (1996, see Fig. 17 therein). This simulation was previously described in Krall et al. (2010a) as an example of

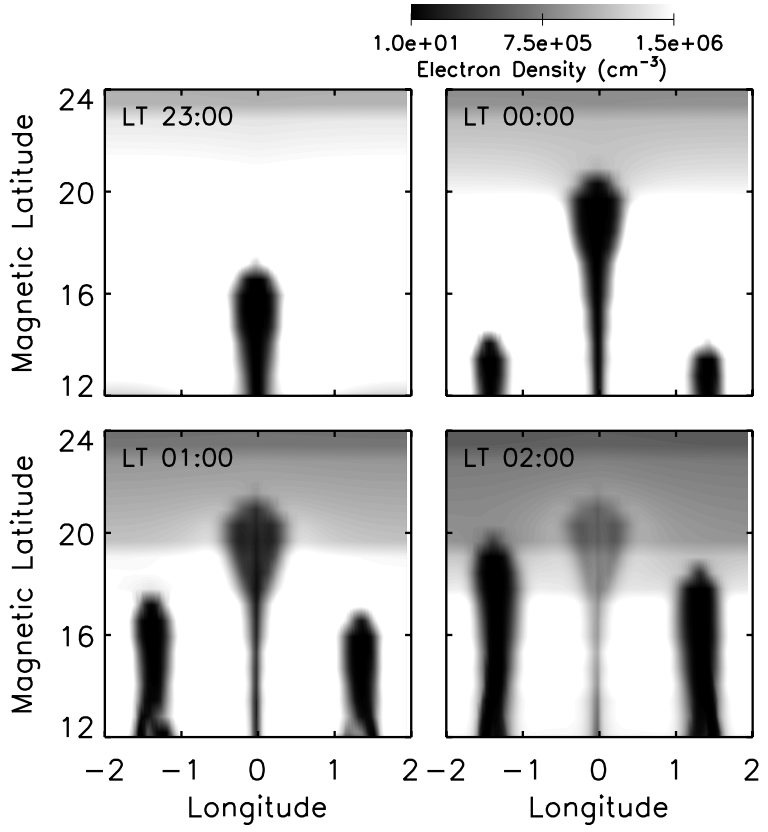

Fig. 6. Electron density versus longitude and latitude at a constant altitude of 288 km at various times. The first three time values correspond to those shown in Fig. 5.

the unusual situation where the ESF "super fountain" (Huba et al., 2009b) is not very strong, leading to "bubbles" that have mild plasma density enhancements ("plasma blobs," see, e.g., Krall et al., 2010a, and references therein) instead of strong depletions at high-altitude.

Results are shown in Figs. 7 and 8 where a selected bubble is viewed in a constant longitude plane as contours of $\log_{10}(n_e)$ (Fig. 7, left-hand panels), as contours of the flux-tube averaged mass density normalized to the O^+ mass $\log_{10}\langle\rho/m_{O^+}\rangle$, the log of the Pedersen conductance $\log(\Sigma_{pp})$, and the electrostatic potential Φ plotted in the equatorial plane (Fig. 7, small panels), and as contours of electron density versus longitude and latitude are plotted at a constant altitude of 288 km (Fig. 8). As in Fig. 1, O^+ motion is shown in Fig. 7 as velocity vectors that indicate the direction of flow *away* from the dot in each case. As in Fig. 3, the location in longitude for each left-hand panel of Fig. 7, is indicated by a vertical line in one of the corresponding plots versus longitude and altitude. As in the previous cases, time values for the three rows of Fig. 7 and the first three panels of Fig. 8 were chosen to show specific states of the evolving bubble: an active bubble, a bubble that has nearly halted, and a fossil bubble that has evolved for some time.

As in all other cases, the upward motion of the ESF plume halts when $\langle\rho\rangle$ values within the apex of the plume are equal to those in the nearby background. Consistent with Chen et al. (1983), an ESF plume in a system with multiple bubbles rises more slowly than in the single-bubble case (Chen et al., 1983, also showed that the fields in a multi-bubble system tend to distort the bubbles, as is seen here). As a result of this weak ESF growth, the super fountain effect is not strong (here the scale of the plotted vectors is only $100\,\mathrm{m\,s^{-1}}$) and there is no plasma density depletion at the apex of the fossil plume. Because of this lack of a high-altitude depletion, and because we see this behaviour only in simulations with both very low $F10.7$ and $F10.7A$ indices and with multiple plumes, we believe this case to be somewhat unusual. Nevertheless, this case is interesting in that both the $\boldsymbol{E}$ field and the full height of the airglow depletion persist through to the near-dawn end of the simulation. This supports the hypothesis, suggested by the previous three simulations, that airglow signatures are associated with field lines where the $\boldsymbol{E}$ field is nonzero.

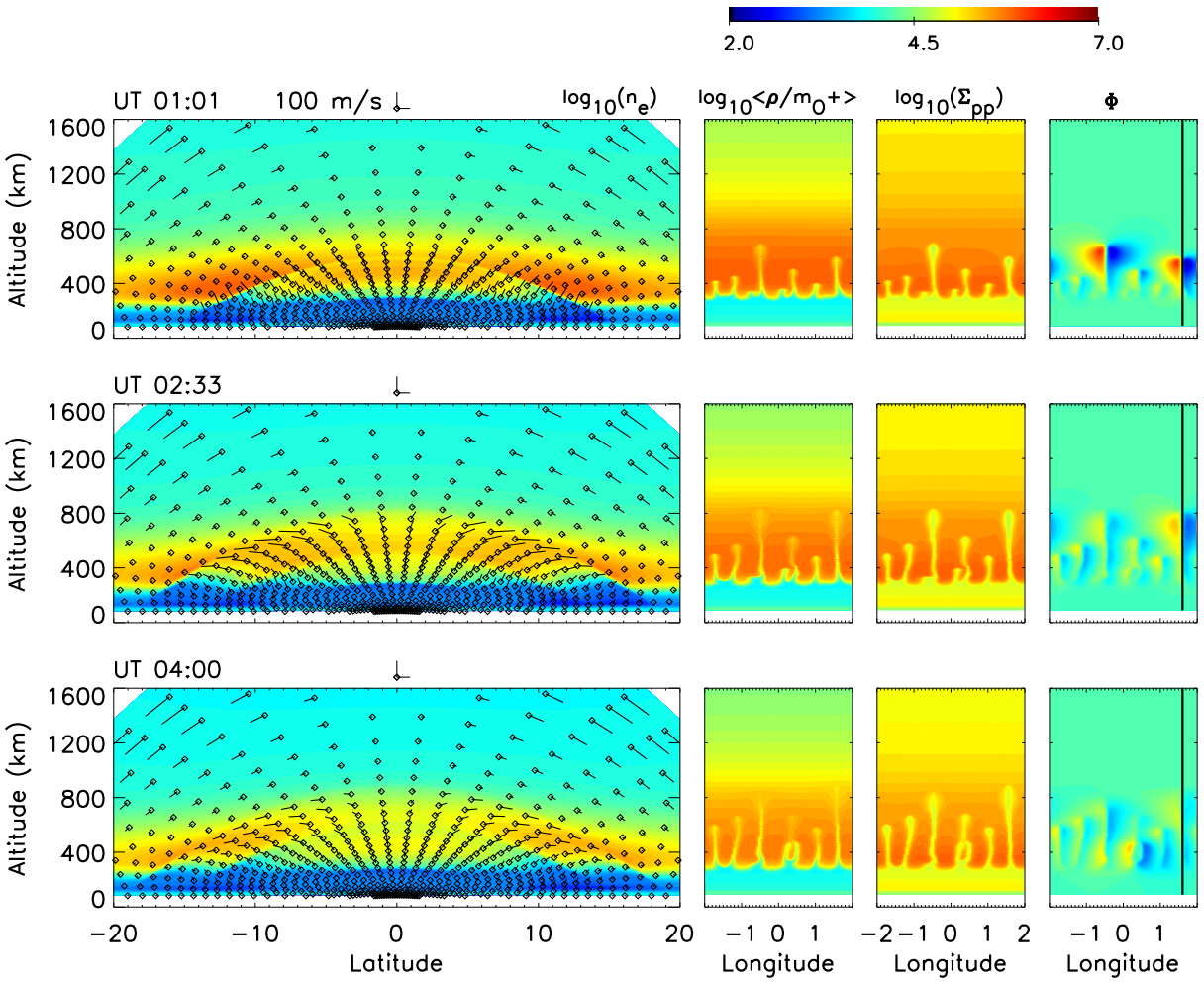

Fig. 7. Left: Contours of $\log_{10} n_e$ versus height and latitude at longitude 1.6° at various times. Right three columns: Contours of the log of the flux-tube averaged ion mass density ($\log_{10}\langle\rho/m_{O^+}\rangle$), the log of the Pedersen conductance ($\log_{10}(\Sigma_{pp})$) and the electrostatic potential, plotted in the equatorial plane. Number densities for n_e, and $\langle\rho/m_{O^+}\rangle$, are in units of cm^{-3} and correspond to the colour-bar scale. In the left hand panels, O^+ ion velocity vectors indicate the direction of flow *away* from the dot. Here there are no winds and the instability is seeded by imposing random fluctuations.

7 Conclusions

We have used the NRL SAMI3/ESF simulation code to examine the behaviour of fossil bubbles in simulations in which we varied either the zonal neutral winds or the initial condition for the instability. These support the previous result of Krall et al. (2010b): in all simulations, ESF plumes stopped rising when the flux-tube-integrated ion mass density inside the upper edge of the bubble was equal to that of the nearby background. We further showed that fossils can persist as high-altitude plasma density depletions even while being "blown" by a zonal wind. Corresponding airglow images of these bubbles, typically observed as light emitted at altitudes of 250–300 km (corresponding to a wavelength of 630.0 nm), are shown to fill in as the $\boldsymbol{E}$ field within the bubble decays to zero and plasma density "falls" down field lines to low altitudes. In particular, field lines that fill in are those upon which the $\boldsymbol{E}$ field has fallen entirely to zero while field lines that do not fill in support a persistent, if weak, $\boldsymbol{E}$ field. Typically, only the higher latitude portion of the airglow depletion signature fills in. However, a plume that has had its upward motion interrupted by a converging zonal wind pattern can have an airglow signature that fills in entirely. In many cases, it is possible to have a fossil plasma density depletion at high altitude (e.g., above the F-layer) on a field line for which the corresponding airglow image shows no depletion.

In these simulations, completely decayed $\boldsymbol{E}$ fields are associated with field lines where the plasma has fallen back to low altitudes, filling in the airglow images and increasing the Pedersen conductance. In related work, Park et al. (2010) has considered the reduction in the $\boldsymbol{E}$ field by a

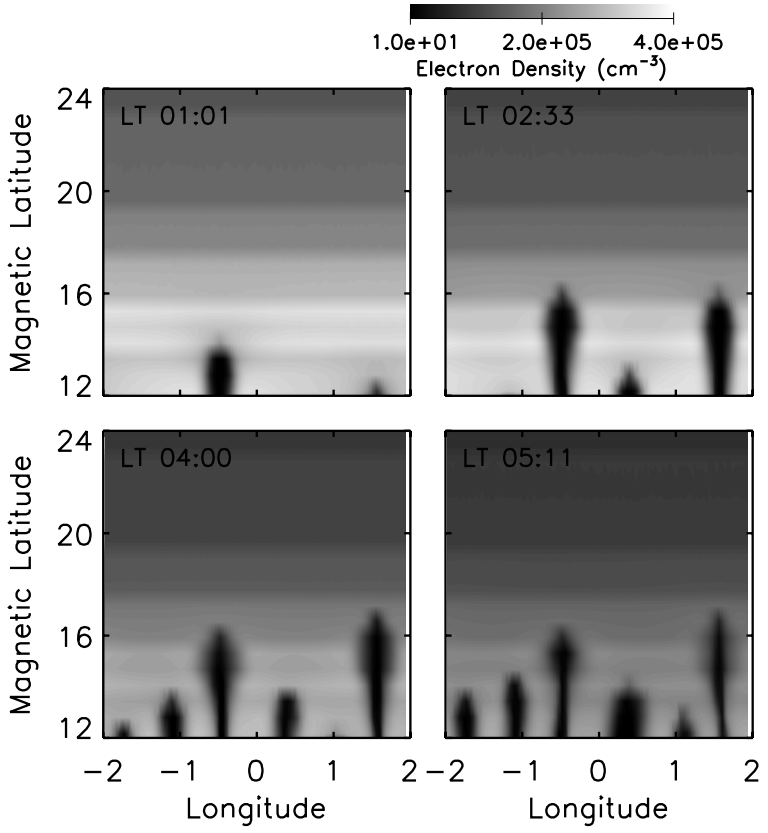

Fig. 8. Electron density versus longitude and latitude at a constant altitude of 288 km at various times. The first three time values correspond to those shown in Fig. 7.

high-conductance region in order to explain observations of "plasma blobs." In that work, there is evidence that field-aligned currents are partially closed across blobs, which are high density regions within an ESF plume (see Krall et al., 2010a, and references within). This leads us to consider the idea that a localized region within an ESF plume with a high value of the Pedersen conductivity can "short out" the $\boldsymbol{E}$ field on coincident field lines within the plume, affecting the dynamics of the plume. However, based on the sequence of events in each simulation, where the bubble stops rising because of conditions at the outward leading edge of the bubble even while $\boldsymbol{E}$ fields within the bubble are quite large, we conclude that any "shorting out" of the field by an increased Pedersen conductance is a secondary effect that occurs after the bubble has stopped rising and has reached a slowly-evolving fossil state.

Acknowledgements. This work was supported by the Office of Naval Research and NASA.

Topical Editor M. Pinnock thanks one anonymous referee for her/his help in evaluating this paper.

References

Abdu, M. A., Iyer, K. N., de Medeiros, R. T., Batista, I. S., and Sobral, J. H. A.: Thermospheric meridional wind control of equatorial spread F and evening prereversal electric field, Geophys. Res. Lett., 33, L07106, doi:10.1029/2005GL024835, 2006.

Argo, P. E. and Kelley, M. C.: Digital ionosonde observations during equatorial spread F, J. Geophys. Res., 91, 5539–5555, 1986.

Booker, H. G. and Wells, H. W.: Scattering of radio waves in the F-region of ionosphere, Terr. Mag. Atmos. Elec., 43, 249–256, 1938.

Chen, J., Satyanarayana, P., and Ossakow, S. L.: The morphology of a multi-bubble system in the ionosphere, J. Geophys. Res., 88, 5528–5536, 1983.

de La Beaujardiere, O., Jeong, L., and The C/NOFS Science Definition Team: C/NOFS: a mission to forecast scintillations, J. Atmos. Sol. Terr. Phys., 66, 1573–1591, 2004.

Haerendel, G.: Theory of equatorial spread F, preprint, Max Planck Inst. Extraterr. Phys., Munich, Germany, 1974.

Haerendel, G., Eccles, J. V., and Çakir, S.: Theory for modeling of the equatorial evening ionosphere and the origin of the shear in the horizontal plasma flow, J. Geophys. Res., 97, 1209–1223, 1992.

Hocke, K. and Schlegel, K.: A review of atmospheric gravity waves and travelling ionospheric disturbances: 1982–1995, Ann. Geophys., 14, 917–940, doi:10.1007/s00585-996-0917-6, 1996.

Huba, J. D. and Joyce, G.: Equatorial spread *F* modeling: multiple bifurcated structures, secondary instabilities, large density 'bite-outs,' and supersonic flows, Geophys. Res. Lett., 34, L07105, doi:10.1029/2006GL028519, 2007.

Huba, J. D. and Joyce, G.: Global modeling of equatorial plasma bubbles, Geophys. Res. Lett., 37, L17104, doi:10.1029/2010GL044281, 2010.

Huba, J. D., Joyce, G., and Fedder, J. A.: SAMI2 (Sami2 is Another Model of the Ionosphere): A New Low-Latitude Ionosphere Model, J. Geophys. Res., 105, 23035–23053, 2000.

Huba, J. D., Joyce, G., Sazykin, S., Wolf, R., and Shapiro, R.: Simulation study of penetration electric fields in the low- to mid-latitude ionosphere, Geophys. Res. Lett., 32, L23101, doi:10.1029/2005GL024162, 2005.

Huba, J. D., Joyce, G., and Krall, J.: Three-dimensional equatorial spread *F* modeling, Geophys. Res. Lett., 35, L10102, doi:10.1029/2008GL033509, 2008.

Huba, J. D., Joyce, G., Krall, J., and Fedder, J.: Ion and electron temperature evolution during equatorial spread-*F*, Geophys. Res. Lett., 36, L15102, doi:10.1029/2009GL038872, 2009a.

Huba, J. D., Krall, J., and Joyce, G.: Atomic and molecular ion dynamics during equatorial spread-*F*, Geophys. Res. Lett., 36, L10106, doi:10.1029/2009GL037675, 2009b.

Huba, J. D., Ossakow, S. L., Joyce, G., Krall, J., and England, S. L.: Three-dimensional spread *F* modeling: Zonal neutral wind effects, Geophys. Res. Lett., 36, L19106, doi:10.1029/2009GL040284, 2009c.

Huba, J. D., Joyce, G., Krall, J., Siefring, C. L., and Bernhardt, P. A.: Self-consistent modeling of equatorial dawn density depletions with SAMI3, Geophys. Res. Lett., 37, L03104, doi:10.1029/2009GL041492, 2010.

Hysell, D. L.: An overview and synthesis of plasma irregularities in equatorial spread *F*, J. Atmos. Sol. Terr. Phys., 62, 1037–1056, 2000.

Kelley, M. C.: The Earth's Ionosphere, Plasma Physics and Electrodynamics, Academic, San Diego, Calif., 1989.

Krall, J., Huba, J. D., Joyce, G., and Zalesak, S. T.: Three-dimensional simulation of equatorial spread-F with meridional wind effects, Ann. Geophys., 27, 1821–1830, doi:10.5194/angeo-27-1821-2009, 2009a.

Krall, J., Huba, J. D., and Martinis, C.: Three dimensional modeling of equatorial spread-*F* airglow enhancements, Geophys. Res. Lett., 36, L10103, doi:10.1029/2009GL038441, 2009b.

Krall, J., Huba, J. D., Joyce, G., and Yokoyama, T.: Density enhancements associated with equatorial spread F, Ann. Geophys., 28, 327–337, doi:10.5194/angeo-28-327-2010, 2010a.

Krall, J., Huba, J. D., Ossakow, S. L., and Joyce, G.: Why do equatorial ionospheric bubbles stop rising?, Geophys. Res. Lett., 37, L09105, doi:10.1029/2010GL043128, 2010b.

Makela, J. J.: A review of imaging low-latitude ionospheric irregularity processes, J. Atmos. Sol. Terr. Phys., 68, 1441–1458, 2006.

Maruyama, T., Saito, S., Kawamura, M., Nozaki, K., Krall, J., and Huba, J. D.: Equinoctial asymmetry of a low-latitude ionosphere-thermosphere system and equatorial irregularities: evidence for meridional wind control, Ann. Geophys., 27, 2027–2034, doi:10.5194/angeo-27-2027-2009, 2009.

Mendillo, M., Baumgardner, J., Pi, X., Sultan, P., and Tsunoda, R.: Onset conditions for equatorial spread *F*, J. Geophys. Res., 97, 13865–13876, 1992.

Ossakow, S. L.: Spread *F* theories: A review, J. Atmos. Terr. Phys., 43, 437–452, 1981.

Park, J., Lühr, H., Stolle, C., Rother, M., Min, K. W., and Michaelis, I.: Field-aligned current associated with low-latitude plasma blobs as observed by the CHAMP satellite, Ann. Geophys., 28, 697–703, doi:10.5194/angeo-28-697-2010, 2010.

Picone, J. M., Hedin, A. E., Drob, D. P., and Aikin, A. C.: NRLMSISE-00 empirical model of the atmosphere: Statistical comparisons and scientific issues, J. Geophys. Res., 107, 1468, doi:10.1029/2002JA009430, 2002.

Retterer, J. M.: Forecasting low-latitude radio scintillation with 3-D ionospheric plume models: 1. Plume model, J. Geophys. Res., 115, A03306, doi:10.1029/2008JA013839, 2010.

Scherliess, L. and Fejer, B. G.: Radar and satellite global equatorial *F* region vertical drift model, J. Geophys. Res., 104, 6829–6842, 1999.

Schunk, R. W. and Sojka, J. J.: Ionosphere-thermosphere space weather issues, J. Atmos. Terr. Phys., 58, 1527–1574, 1996.

Sekar, R., Chakrabarty, D., Sarkhel, S., Patra, A. K., Devasia, C. V., and Kelley, M. C.: Identification of active fossil bubbles based on coordinated VHF radar and airglow measurements, Ann. Geophys., 25, 2099–2102, doi:10.5194/angeo-25-2099-2007, 2007.

Steenburgh, R. A., Smithtro, C. G., and Groves, K. M.: Ionospheric scintillation effects on single frequency GPS, Space Weather, 6, S04D02, doi:10.1029/2007SW000340, 2008.

Yokoyama, T., Su, S.-Y., and Fukao, S.: Plasma blobs and irregularities concurrently observed by ROCSAT-1 and Equatorial Atmosphere Radar, J. Geophys. Res., 112, A05311, doi:10.1029/2006JA012044, 2007.

Zalesak, S. T., Ossakow, S. L., and Chaturvedi, P. K.: Nonlinear equatorial spread *F*: The effect of neutral winds and background Pedersen conductivity, J. Geophys. Res., 87, 151–166, 1982.